Imaging Sensor Constellation for Tomographic Chemical Cloud Mapping

Bogdan R. Cosofret,[1,*] Daisei Konno,[1] Aram Faghfouri,[1] Harry S. Kindle,[1]

Christopher M. Gittins,[1] Michael L. Finson,[1] Tracy E. Janov,[1] Mark J. Levreault,[2]

Rex K. Miyashiro,[3] and William J. Marinelli[1]

[1]*Physical Sciences Inc., 20 New England Business Center, Andover, MA, USA 01810-1077*

[2]*Vtech Engineering Corporation, 20 New England Business Center, Andover, MA, USA 01810-1077*

[3]*Research Support Instruments, 4325B Forbes Blvd., Lanham, MD USA, 20706*

[*]*Corresponding author: cosofret@psicorp.com*

Report Documentation Page		*Form Approved* *OMB No. 0704-0188*

Public reporting burden for the collection of information is estimated to average 1 hour per response, including the time for reviewing instructions, searching existing data sources, gathering and maintaining the data needed, and completing and reviewing the collection of information. Send comments regarding this burden estimate or any other aspect of this collection of information, including suggestions for reducing this burden, to Washington Headquarters Services, Directorate for Information Operations and Reports, 1215 Jefferson Davis Highway, Suite 1204, Arlington VA 22202-4302. Respondents should be aware that notwithstanding any other provision of law, no person shall be subject to a penalty for failing to comply with a collection of information if it does not display a currently valid OMB control number.

1. REPORT DATE **30 JAN 2009**	2. REPORT TYPE	3. DATES COVERED **00-00-2009 to 00-00-2009**
4. TITLE AND SUBTITLE **Imaging Sensor Constellation for Tomographic Chemical Cloud Mapping**		5a. CONTRACT NUMBER
		5b. GRANT NUMBER
		5c. PROGRAM ELEMENT NUMBER
6. AUTHOR(S)		5d. PROJECT NUMBER
		5e. TASK NUMBER
		5f. WORK UNIT NUMBER
7. PERFORMING ORGANIZATION NAME(S) AND ADDRESS(ES) **Physical Sciences Inc,20 New England Business Center,Andover,MA,01810-1077**		8. PERFORMING ORGANIZATION REPORT NUMBER
9. SPONSORING/MONITORING AGENCY NAME(S) AND ADDRESS(ES)		10. SPONSOR/MONITOR'S ACRONYM(S)
		11. SPONSOR/MONITOR'S REPORT NUMBER(S)

12. DISTRIBUTION/AVAILABILITY STATEMENT
Approved for public release; distribution unlimited

13. SUPPLEMENTARY NOTES

14. ABSTRACT

15. SUBJECT TERMS

16. SECURITY CLASSIFICATION OF:			17. LIMITATION OF ABSTRACT	18. NUMBER OF PAGES	19a. NAME OF RESPONSIBLE PERSON
a. REPORT **unclassified**	b. ABSTRACT **unclassified**	c. THIS PAGE **unclassified**	**Same as Report (SAR)**	**46**	

Imaging Sensor Constellation for Tomographic Chemical Cloud Mapping

Bogdan R. Cosofret,[1,*] Daisei Konno,[1] Aram Faghfouri,[1] Harry S. Kindle,[1]

Christopher M. Gittins,[1] Michael L. Finson,[1] Tracy E. Janov,[1] Mark J. Levreault,[2]

Rex K. Miyashiro,[3] and William J. Marinelli[1]

[1]*Physical Sciences Inc., 20 New England Business Center, Andover, MA, USA 01810-1077*

[2]*Vtech Engineering Corporation, 20 New England Business Center, Andover, MA, USA 01810-1077*

[3]*Research Support Instruments, 4325B Forbes Blvd., Lanham, MD, USA 20706*

[*]*Corresponding author: cosofret@psicorp.com*

A sensor constellation capable of determining the location and detailed concentration distribution of chemical warfare agent simulant clouds has been developed and demonstrated on government test ranges. The constellation is based on the use of standoff passive multispectral infrared imaging sensors to make column density measurements through the chemical cloud from two or more locations around its periphery. A Computed Tomography (CT) inversion method is employed to produce a three dimensional concentration profile of the cloud from the two-dimensional line density measurements. In this paper, we discuss the theoretical basis of the approach and present results of recent field experiments where controlled releases of chemical warfare agent simulants were simultaneously viewed by three chemical imaging sensors. Systematic investigations of the algorithm using synthetic data indicate that for complex functions, 3-D reconstruction errors are less than 20% even in the case of a limited 3-sensor measurement network. Field

data results demonstrate the capability of the constellation to determine 3-D concentration profiles that account for ~<86%> of the total known mass of material released.

OCIS codes: 280.0280, 280.4991

1.   Introduction

The improvement of ground test validation capability in the form of rapid and accurate evaluation of sensor technologies has recently been targeted by the Joint Program Executive Office for Chemical and Biological Defense (JPEO-CBD) as an important technical objective [1]. The goal of the effort reported in this paper is to develop a system that is capable of providing accurate three dimensional concentration distributions of chemical warfare agent simulant clouds released on test ranges. Such a system enhances the ability to validate new chemical and biological sensing technology, as well as provides a better understanding of the fate and transport of chemical releases through chemical reaction models. Currently employed technology serving this purpose makes use of single pixel passive Fourier Transform Infrared (FTIR) spectrometers which scan a viewing area every 15 seconds [2]. Information on the column density of the chemical cloud obtained from the FTIR units is coupled to data provided by point sensors located across the test area. The majority of this information is not currently available for near-real time processing and is collected manually after a test is completed. One goal of this effort is the development of capability to provide the concentration profiles in real time as well as specific data presentation approaches to enable rapid evaluation of the performance of systems under test.

The method of computed tomography (CT) allows the three dimensional reconstruction of a chemical cloud density distribution from a series of two dimensional measurements of the line of sight column density through the cloud at different viewing angles. The use of CT with multispectral passive infrared measurements of individual components in a chemical cloud parallels the approach used in X-ray based medical imaging and can be an important tool in understanding chemical cloud dynamics.

In this paper, we describe the development and application of an imaging sensor constellation for tomographic chemical cloud mapping that provides near-real time detection, tracking and full 3-D concentration information on chemical clouds, both in test situations as well as potentially during emergency events. We utilize the results of chemical imaging experiments conducted during the summer of 2006 employing three LWIR imaging Fabry-Perot spectrometers developed by Physical Sciences Inc. (PSI) to evaluate the performance of the system. The instrument is known as an Adaptive InfraRed Imaging Spectroradiometer, *AIRIS*™ (U.S. Patent 5,461,477). The experiments involved imaging a series of controlled chemical vapor releases at Dugway Proving Ground (DPG). An illustration of the system configuration is shown in Figure 1. The field study was focused on the dissemination of several chemical warfare agent simulants viewed from three fixed locations approximately 2.8 km away from the release point.

Passive sensing of chemical vapor clouds relies on both the spectral signatures of the target species as well as the radiance contrast between the vapor and the background scene. The AIRIS sensor units are comprised of a long wave infrared (LWIR) focal plane array-based camera which views the far field through a low-order, tunable Fabry-Perot etalon [3,4]. The tunable etalon provides the spectral resolution necessary to resolve structured absorption and emission from molecular vapors. The focal plane array (FPA) enables radiance measurements of

sufficient sensitivity that the species-specific column densities of chemical clouds may be determined with only a couple of degrees effective temperature difference between the vapor and the background. We present a synopsis of the development of the PSI tomographic system by first describing results obtained using synthetic data. This exercise has allowed us to better understand the absolute capability of the algorithm in the case of limited measurement network (only three sensors). Finally, we present the results obtained from the tomographic analysis of the infrared imagery from the DPG disseminations.

2. Experimental Configuration and Theoretical Basis of the Approach

2.1 AIRIS Sensor Technology

The AIRIS-Wide Area Detector (WAD) instrument has been described in detail elsewhere [5,6]. The basic AIRIS optical configuration is shown in Figure 2. The concept is based on the insertion of a tunable Fabry-Perot interferometer (etalon) into the field-of-view of an infrared focal plane array (FPA). The IR FPA views the far field through the piezoelectric-actuated etalon placed in an afocal region of the optical train. The tunable etalon is operated in low order (mirror spacing comparable to the wavelength of the light transmitted) and functions as an interference filter which selects the wavelength viewed by the FPA. The optical configuration depicted in Figure 2 affords a wide field of view, high optical throughput, and broad wavelength coverage at high spectral resolution. The interferometer tuning time is ~2 ms between transmission wavelengths. Fore-optics and integrated blackbody calibration sources, not depicted in Figure 2, enable control of the sensor's field-of-regard and absolute radiometric calibration of the data. The AIRIS units operated in the study provided 256 pixel x 256 pixel

imagery at 2.2 x 2.2 mrad IFOV per pixel. This configuration resulted in a 32 degree x 32 degree field of regard.

The three AIRIS units were configured to acquire imagery between 7.9 and 11.2 μm at ~0.08 μm (8 cm^{-1}) spectral resolution. The AIRIS FPA acquires frames at 200 Hz and typically 8 frames were averaged at each observation wavelength. The etalon tuning time to observation wavelengths is much less than the FPA framing period and the typical datacube acquisition time was ~0.8 seconds. Datacubes were acquired once every ~1.7 seconds. The noise equivalent spectral radiance (NESR) of the data was ~1.5 μW cm^{-2} sr^{-1} μm^{-1} (μFlicks) over the entire operating range and is equivalent to a noise-equivalent temperature difference ~0.1 K. Radiometric calibration of the data was accomplished using a two point gain and offset correction using internal blackbody calibration sources set for two temperatures: T_{cold} ~ 288 K, and T_{hot} ~ 308 K. A calibration of the system was executed once every 30 minutes for accurate radiometric measurements. The spectral radiance of ambient temperature objects was typically ~800 μW cm^{-2} sr^{-1} μm^{-1} over the typical field temperature range and the change in radiance with temperature is ~15 μW cm^{-2} sr^{-1} μm^{-1} K^{-1}. Each 256 pixel × 256 pixel × 20 wavelength AIRIS datacube is used to create a 256 pixel × 256 pixel array of chemical vapor column density values using the approach described below.

2.2   Radiative Transfer and Sensor Signal Model

The detection approach is based on the change in passive infrared radiation received by the spectrally resolving sensor due to the presence of a chemical cloud. The basic process can be described by a three layer model, as shown by Flanigan [7] and is illustrated in Figure 3. The total infrared radiance incident on the sensor at a given wavelength is the sum of the contributions from each layer and is given by:

$$N_{sensor}(\lambda) = t_A \bullet t_C \bullet N_B(\lambda,T_1) \bullet \varepsilon_B(\lambda) + t_A \bullet [1-t_C] \bullet N_C(\lambda,T_2) + [1-t_A] \bullet N_A(\lambda,T_3) \quad (1)$$

where $N_B\varepsilon_B$ is the Planck radiance of the background, N_C is the Planck function radiance at the thermodynamic temperature of the chemical cloud, and N_A is the Planck function radiance at the thermodynamic temperature of the atmosphere. The quantities t_C and t_A are the spectral transmission of the cloud and the atmosphere between the cloud and the sensor, respectively. The first term in Eq. (1) describes the radiance from the background as attenuated by the chemical cloud and intervening atmosphere. The second term describes the radiance of the chemical species in the cloud as attenuated by the atmosphere between the cloud and the sensor. Finally, the third term in Eq. (1) describes the radiance of the atmosphere between the cloud and the sensor. The transmission of the cloud, layer 2, is computed from the spectral properties of the chemical species contained therein:

$$
\begin{aligned}
t_C(\lambda) &= \exp[-\sum \sigma_i(\lambda)\rho_i] \\
\rho_i &= C_i \ell
\end{aligned}
\quad (2)
$$

where C_i is the average concentration of the chemical compound over the line of sight through the cloud, ℓ (ρ_i is the chemical column density) and $\sigma_i(\lambda)$ is the wavelength-dependent absorption coefficient. The sum over index i in Eq. (2) is over all spectrally relevant chemical species.

The differential radiance observed by the sensor as a result of the presence of the chemical cloud can be approximated as:

$$\Delta N(\lambda) = [t_A \bullet t_C \bullet N_B(\lambda,T_1) \bullet \varepsilon_B(\lambda) + t_A \bullet [1-t_C] \bullet N_C(\lambda,T_2) + [1-t_a] \bullet N_A(\lambda,T_3)] - \hat{N}(\lambda) \quad (3)$$

where $\hat{N}(\lambda)$ is the radiance measured at the sensor in the absence of the chemical cloud ($t_C \rightarrow$ 1) and is defined as:

$$\hat{N}(\lambda) = t_A \bullet N_B(\lambda, T_1) \bullet \varepsilon_B(\lambda) + [1 - t_a] \bullet N_A(\lambda, T_3) \tag{4}$$

In order to determine the chemical simulant spectral transmission, t_C from measured sensor radiometrics, and therefore obtain its column density, we make use of a fundamental assumption: we assume that the chemical cloud attains atmospheric temperature due to rapid mixing with the surrounding air. This assumption allows for the approximation that $N_C \approx N_A$ and N_A can be determined from a measurement of the local air temperature. Furthermore, to first order, this assumption also relaxes the need to have implicit knowledge of the atmospheric attenuation, t_A between the cloud and the sensor. This approach has been used in previous work [8]. We note that atmospheric temperature generally decreases with increasing height above ground level and that for clouds which rise high (several hundred meters) above the ground, it is necessary to address the decrease in air temperature with altitude as the cloud mass will be underestimated if the cloud temperature is presumed to be equal to the ground-level atmospheric temperature. The majority of the concentration profiles estimated in this work are calculated for elevations within tens of meters of the ground however, so we do not address variation of air temperature with altitude here.

With the assumption that the cloud temperature is equal to the ambient air temperature, the cloud transmission can be determined from Eq. (1) and Eq. (4) as follows:

$$t_C(\lambda) = \frac{N_{sensor}(\lambda) - N_A(\lambda)}{\hat{N}(\lambda) - N_A(\lambda)} \tag{5}$$

where N_{sensor} is the sensor measurement, and N_A is the Planck radiance for a blackbody at ambient air temperature, which can be measured locally. The temperature values are typically obtained from a weather station which is positioned in proximity to the chemical release.

The most complex problem left to be addressed in order to solve Eq. (5) is the determination of $\hat{N}(\lambda)$, the scene radiance in the absence of the chemical cloud. As a result of the fact that we do not have *a priori* knowledge of the background characteristics (spectral features and temperature, T_1), and as a result of the constant change of the background temperature with time, we utilize statistical methods for the determination of $\hat{N}(\lambda)$. This approach allows for the identification of detector pixels containing the chemical simulant, as well as the calculation of the radiance in the absence of the chemical cloud even when the simulant cloud is present in the field of view. The mathematical underpinnings of this analysis method are described below.

The Adaptive Cosine Estimator (ACE)–based approach to target detection is described in more detail elsewhere [9]. ACE follows from an "unstructured background" model. The unstructured background model assumes that, while one can determine an average spectrum for a background type, there is inherent spectral variability within the material type and that, with the exception of lucky coincidences, one cannot accurately represent a measured spectrum by a linear combination of the average spectra of each material type (as is commonly used in Subspace-Generalized Likelihood Ratio Test approach [9]). For the field data that we have investigated to date, the unstructured background model appears to provide a better estimate of the observed backgrounds than Subspace-GLRT approaches. Within this model, the spectra of background pixels are described as random vectors whose likelihood of occurrence is described

by a probability distribution function. The unstructured background model can be described by the following expression:

$$\underline{x} = \mu + S\alpha + \nu \tag{6}$$

where $\underline{\mu}$ is the mean spectrum of the spectral/spatial datacube, S is a reference spectrum (absorption coefficients) for the chemical vapor of interest, and ν is a random vector which is characterized by a probability distribution function. The parameter $S\alpha$, as defined in Eq. (6), is the differential radiance spectrum due to the presence of the chemical cloud as expressed in Eq. (3). In the event that ν is normally-distributed or elliptically-distributed, Eq. (6) can be expressed in terms of a noise-whitened variable:

$$\underline{z} = \underline{\underline{\Gamma}}^{-1/2}(x - \mu) = \underline{\underline{\Gamma}}^{-1/2}S\alpha + n \tag{7}$$

where $\underline{\underline{\Gamma}}$ is the covariance matrix of the non-target-containing pixels and n is a random vector whose elements, when averaged over the entire datacube, have zero mean and unit standard deviation. By working in a noise-whitened space, bands with low signal-to-noise are de-weighted in the analysis and bands with high signal-to-noise receive proportionally higher weight.

Following Eq. (7), the ACE detection metric is:

$$D_{ACE}(\underline{z}) = \frac{\underline{z}^T \left(\underline{\underline{\Gamma}}^{-1/2}S\right)\left(S^T \underline{\underline{\Gamma}}^{-1}S\right)^{-1}\left(\underline{\underline{\Gamma}}^{-1/2}S\right)^T \underline{z}}{\underline{z}^T \underline{z}} \tag{8}$$

Values of D_{ACE} range from zero to unity, where unity indicates perfect correlation between the test spectrum and the target spectrum and zero indicates no correlation. "Target present" is declared when D_{ACE} exceeds a user-specified threshold. One of the practical challenges in

applying ACE is determining which pixels in the scene to use to calculate μ and $\underline{\underline{\Gamma}}$. Eq. (7) may

be inverted to calculate target spectrum amplitudes. Pixels exhibiting anomalously large values

of Mahalanobis distance, typically values greater than that which would lead to inclusion of 99%

of data from a multivariate normal distribution, are identified and the mean and covariance are

recalculated with those points excluded. In practice, when the cloud occupies a small fraction of

the scene, nominally a several percent of the pixels or less, this method of estimating the

background mean and covariance has the effect of excluding most of the target-signature-

containing pixels.

The least-squares-optimum estimate of target signature amplitude is:

$$\hat{\alpha} = \left(S^T \underline{\underline{\Gamma}}^{-1} S\right)^{-1} \left(S\right)^T \underline{\underline{\Gamma}}^{-1}(x - \mu)$$

(9)

Based on Eq. (9), the differential radiance spectrum resulting from the presence of the

chemical in the field of view of the sensor ($\Delta N = S\hat{\alpha}$) is determined for each datacube

acquisition and for each pixel satisfying the D_{ACE} user-specified threshold. Consequently, the

radiance at the sensor in the absence of the chemical cloud is calculated as follows:

$$\hat{N}(\lambda) \approx N_{sensor}(\lambda) - S\hat{\alpha}$$

(10)

where $N_{sensor}(\lambda)$ is the measured radiance spectrum and $S\hat{\alpha}$ is the best fit to the model as defined

above. Equation (10) can be used directly in conjunction with Eq. (5) to calculate the cloud

transmission for each pixel identified as containing the chemical simulant. Finally, following

Eq. (2), the chemical simulant column density (ρ_i) of chemical species i is calculated as:

$$\hat{\rho}_i = \hat{\alpha}_i \cdot \frac{\langle \partial L / \partial T \rangle}{\langle N_A - (N_{sensor} - S\hat{\alpha}) \rangle} \tag{11}$$

where $\langle \partial L / \partial T \rangle$ is the derivative Planck function with respect to temperature averaged over the wavelengths in the datacube and $\langle N_A - (N_{sensor} - S\hat{\alpha}) \rangle$ is the average differential radiance between a blackbody at the air temperature and the estimated background spectrum.

The capability of the detection approach to accurately measure the chemical column density was initially validated under controlled conditions in the laboratory. The laboratory testing involved observing varying concentrations of a chemical in an absorption cell of known length viewed against a blackbody of known temperature. The cell was filled with a given mixture ratio of 1,1,1,2-tetrafluoroethane (R134a)/nitrogen, such that column densities of 100-500 mg/m^2 were achieved. Directly behind the absorption cell, a large surface area blackbody was heated in order to achieve a temperature differential of ~ 3 °C with respect to the ambient temperature. Data was acquired for several R134a column densities, and the imagery was processed according to the principles described above. Figure 4 illustrates R134a identification for all pixels inside the absorption cell. Figure 5 shows the comparison between the known column density and the calculated chemical column density based on the application of Eq. (11). Results indicate that errors associated with ACE-based column density estimation are less than 10% when the uncertainty in the ambient temperature measurement is ~ ± 0.3°C.

The primary error contributions to the chemical cloud density measurement are defined through a simple error propagation analysis of Eq. (11). The uncertainty in the column density value is evaluated as follows:

$$\sigma_\rho{}^2 = \left(\frac{\partial\rho}{\partial\alpha}\right)^2 \sigma_\alpha{}^2 + \left(\frac{\partial\rho}{\partial N_{sensor}}\right)^2 \sigma_{N_{sensor}}{}^2 + \left(\frac{\partial\rho}{\partial N_A}\right)^2 \left(\frac{\partial N_A}{\partial T_A}\right)^2 \sigma_{T_A}{}^2 \qquad (12)$$

where σ_α is the uncertainty in the ACE-based statistical estimate of the target spectrum amplitude, $\sigma_{Nsensor}$ is the error associated with the sensor radiometric measurement (results from the uncertainty associated with the radiometric calibration of the sensor as well as the sensor Noise Equivalent Spectral Radiance (NESR)), and σ_{TA} is the uncertainty in the ambient temperature measurement. Figure 6 illustrates the overall error contributions from each of these elements under typical measurement conditions. In a field deployment situation, where a single weather station can be positioned some distance away from the actual chemical cloud, the uncertainty in the ambient temperature measurement can easily approach ± 1.0°C. Consequently, it can be observed from Figure 6 that the uncertainty associated with the temperature measurement introduces the largest error (~17 µFlicks) to the overall sensor radiometric measurements.

3. Computed Tomography Algorithm for use with Passive Standoff Detection of Chemical Clouds

Combinations of an integrating measurement technique and CT have been used in many different fields for the study of diverse phenomena [10]. Several examples include measurement of soot volume fractions in a flame based on integrated light absorption measurements [11], measurement of plasma emission intensity distributions by use of integrated emission measurements [12], and measurement of density distributions in fluid flows by use of interferometry via integration of the refractive index [13].

The most difficult problem for optical tomography as applied to chemical cloud concentration mapping is the lack of sufficient projection data for reconstruction; it is not

feasible (cost prohibitive) to acquire column density from the cloud using very many sensors. The ability to provide a good tomographic reconstruction of a chemical cloud is dependent on the number of sensors used as well as the geometric positioning of the sensors. The quality of the reconstruction as a function of these parameters was a primary focus in determining the tomographic method used for the system.

We are given a number of optical density projections $\psi_p(x,z) \equiv \rho\ (\psi_p(x,z))$, where ψ_p is the column density measurement at each pixel identified as containing the simulant in the 2-D plane orthogonal to the sensor line of sight, and from which the chemical cloud concentration function $C(x,y,z)$ is to be reconstructed:

$$\Psi_p(x,z) \equiv \int_0^L C(x,y,z)dy \tag{13}$$

where the integration is along the line of sight y. Therefore, given ψ_p for p=1,….,P one needs to find an estimate of $C(x,y,z)$. The full 3-D $C(x,y,z)$ is generated by stacking each of the reconstructed 2-D concentration distributions, $C(x,y)$. Many algorithms have been developed for the reconstruction process, and the choice of usage is governed by factors such as computational power and speed, as well as the spacing and projection data available. The choice of CT algorithm for our application was based on the need to generate the highest fidelity reconstructions with limited projection data and without any *a priori* knowledge of the chemical cloud concentration distribution. There are generally two types of CT algorithms that have been extensively used in the physical sciences: transform based and series-expansion based.

The transform algorithms are based on the Fourier and Radon transforms. The Fourier algorithms make use of the projection (or central-section) theorem [14], which relates the

one-dimensional Fourier transform of a projection of an object to the two-dimensional transform of the object itself. In a limited projection data case however, there are gaps in the transform information that must be filled before the inverse transformation can provide a reasonable reconstruction of the original object [10]. The Radon transform-based reconstruction algorithms are iterative methods similar to the Fourier approaches but with the iteration carried out between the object domain and the Radon (projection) domain. Support and range constraints are applied on the object in the spatial domain, and the measured projections are injected at each iteration into the projection space [10]. The transformations are carried out by projection and filtered backprojection. The fundamental problem with transform-based algorithms is that they implicitly assume that the number of projections is very large. Feng *et al.* [15] proposed an optimization approach to try to do a reconstruction from only 3 separate projection views. This approach however, works only for continuous and smooth object density functions. Furthermore, the algorithms require the line integrals to be taken along uniformly spaced and parallel projections. Even though transform-based algorithms are computationally very fast, their limitations in dealing with reduced projection data fields do not make them good candidates for use in the application proposed in this paper.

A better solution to the reconstruction of chemical clouds interrogated by only a few sensors is accomplished via the use of expansion-based algorithms. In the series-expansion formalism, $C(x,y,z)$ is modeled as a linear combination of object coefficients, each of which corresponds to the value of the chemical cloud concentration at a point on a rectangular grid. Expansion algorithms are iterative methods that divide the volume of interest into voxels, and one tries to assign a concentration value to each voxel in such a way that the inferred path

integrals match the observed integrals. The mathematical definition of the algorithm is as follows [10]:

$$\Psi_p = \sum_j^{MNQ} O_j \int_s b_p(x - x_j, y - y_j, z - z_j)ds \qquad (14)$$

where Oj is the jth object concentration value corresponding to position (x_j, y_j, z_j) in the reconstruction space and b is a basis function that weights the contribution of each voxel. The (x_j, y_j, z_j) positions form a rectangular space with M(x direction), N (y direction), Q (z-direction) sides. The (x, z) plane is the plane of the column density image and the integral is along y. Eq. (14) can be written in simple matrix form, ψ = WO:

$$\begin{bmatrix} \Psi_p \end{bmatrix} = \begin{bmatrix} W_{ij} \end{bmatrix} \begin{bmatrix} O_p \end{bmatrix} \qquad \begin{matrix} \text{Where:} & \Psi = \text{Measurement Vector} \\ & W = \text{Projection Matrix} \\ & O = \text{Object Vector} \end{matrix} \qquad (15)$$

where O_j is the local value of the object field C(x,y,z) at the jth voxel, and w_{ij} is the weighting factor which relates the proportion of the jth voxel being interrogated by the finite width. The projection matrix is determined by the number of sensors and the sensor positioning geometry used in the measurement. The column density inferred from a single sensor measurement along a viewing projection is thus defined as a summation of the concentration values for all voxels that are intersected by that projection weighted by the fraction of each voxel intersected by an individual sensor pixel *i*FOV. While the sensors provide fan beam projections through the volume of interest, because the cloud is in the far field and we are only interested in estimating the concentration field over a narrow range of elevation angles near horizontal, we approximate

15

the 3-D distribution as a stack of non-interacting 2-D horizontal layers and the CT algorithm is applied separately to each layer in order to simplify the calculation. Within each 2-D horizontal layer however, each viewing projection incorporates a fan beam approach. This procedure is illustrated in Figure 7.

In the formalism defined by Eq. (15), one would like to solve the set of P linear algebraic equations (one equation for each measured line integral) in MNQ unknowns. Equation (15) may suggest that in order to determine concentration values (O_j) one would only need to do a straight forward matrix inversion. However, one needs to consider some important factors: 1) the number of projections must be the same as the number of cells, 2) for cases where there are more unknowns than equations, conventional matrix inversion is no longer possible, and 3) if the data suffers from the usual random fluctuations and noise, an exact solution will not be possible. Clearly, in the case of limited measurement network (limited number of sensors), the system defined by Eq. (15) is severely under-defined. There are several methods that can be applied in order to provide the best solution to such a system.

In the Algebraic Reconstruction Technique (ART), the solution to the matrix equation is established through an iterative process, in which, an initial estimate of C(x,y) for each cell in a single plane is given, followed by a calculation of the column density, Ψ_p, which is compared to the measured value for the projection. A correction to the initial value of C(x,y) is then performed, and the process is repeated until a given convergence criteria is achieved. The ART technique is a widely used reconstruction method and is generally simple and flexible. Verhoeven [10] presented a study on the effectiveness of this algorithm and looked at its reconstruction ability by investigating the reconstruction of three simulated objects from three

16

different geometries. His conclusion was that the best reconstruction is produced in the geometry including fewer views, but which are spread over a larger angle.

There are several other expansion-based algorithms that attempt to solve the matrix equation. According to work by Todd *et al.* [16], reconstructions performed by Maximum Likelihood Expectation Maximization (MLEM) technique are found to be statistically better than ART. MLEM is a simultaneous method. At each iteration, all voxels are corrected simultaneously after reading an entire set of beam projection data. The tomography reconstruction algorithm that we implemented for use with IR passive standoff detection of chemical clouds is a combination of the ART and MLEM techniques. The formalism follows Eq. (15) and the correction (update) to $C(x,y)$ in each iteration is determined by maximizing the log-likelihood function of observing a given line integral through the cloud. The mathematical underpinnings of the approach are described below.

Let us define $C(x_j, y_j, z_j) = O_j$, as the object concentration value at the jth voxel, as suggested previously. In this case, for each voxel, there is a Poisson distributed random variable O_j, with mean $\overline{O_j}$ that can be generated independently (While the presumption that projection measurements follow Poisson statistics is not rigorously correct for the column densities estimated here, in practice it appears to be a reasonable assumption and it has the benefit of constraining estimated concentration values to be greater than zero.):

$$P(O_j) = e^{-\overline{O_j}} \frac{\overline{O_j}^{O_j}}{O_j!} \tag{17}$$

The jth voxel produces a line integral at ψ_p, which is an independent Poisson variable with an expectation value defined as (the projection of the estimated optical density vector):

$$\tilde{\psi}_p = \sum_{j}^{MNQ} w_{pj} O_j \qquad (18)$$

w_{pj} is the probability (projection) matrix identical to the transfer matrix from voxel j to the set of parallel projections p (defined in Eq. (15)). Since O_j are independent variables, a linear combination of these two variables follows Poisson statistics. Therefore, the likelihood of the observed data is:

$$P(\psi_p) = \prod_{p=1}^{P} e^{-\tilde{\psi}_p} \frac{\tilde{\psi}_p^{\psi_p}}{\psi_p!} \qquad (19)$$

In other words, this is the probability under the Poisson model that the given line integrals Ψ_p are observed if the true optical density is O_j.

The log-likelihood function under MLEM formalism is then defined as:

$$\ln(P(\psi_p)) = -\sum_{p=1}^{P} (\tilde{\psi}_p) + \sum_{p=1}^{P} \ln(\frac{\tilde{\psi}_p^{\psi_p}}{\psi_p!}) = -\sum_{p=1}^{P} (\tilde{\psi}_p) + \sum_{p=1}^{P} \psi_p \ln(\tilde{\psi}_p) - \sum_{p=1}^{P} \ln(\psi_p)$$

$$= -\sum_{p=1}^{P} \sum_{j}^{MNQ} w_{pj} O_j + \sum_{p=1}^{P} \psi_p \ln(\sum_{j}^{MNQ} w_{pj} O_j) - \sum_{p=1}^{P} \ln(\psi_p) \qquad (20)$$

MLEM tries to maximize the function in Eq. (20). In order to do this maximization, one looks at the first derivative of the function with respect to O_j, and solves the equation when the derivative is zero. Thus:

$$\frac{\partial}{\partial O_j}[\ln(P(\psi_p))] = -\sum_{p=1}^{P} \sum_{j=1}^{MNQ} w_{pj} + \sum_{p=1}^{P} \frac{\psi_p}{\sum_{j=1}^{MNQ} O_j} = 0 \qquad (21)$$

Dividing all sides by $-\sum_{p=1}^{P}\sum_{j=1}^{MNQ}w_{pj}$, then multiplying by O_j and combining with Eq. (18) one gets:

$$O_j^{n+1} = \sum_{p=1}^{P}\frac{\psi_p O_j w_{pj}}{\sum_{j=1}^{MNQ}w_{pj}O_j} = O_j^n\sum_{p=1}^{P}\frac{\psi_p w_{pj}}{\sum_{j=1}^{MNQ}w_{pj}O_j} = O_j^n\frac{\sum_{p=1}^{P}w_{pj}\dfrac{\psi_p}{\tilde{\psi}_p}}{\sum_{j}w_{pj}} \qquad (22)$$

Eq. (22) defines the basis for the tomographic reconstruction. $\tilde{\psi}_p$ is the projection of the

estimated concentration vector O at a given iteration n. Let $T^n = \dfrac{\sum_{p=1}^{P}w_{pj}\dfrac{\psi_p}{\tilde{\psi}_p}}{\sum_{j}w_{pj}}$, then $O_j^{n+1} = O_j^n T_j^n$

where T is the multiplicative coefficient that updates the value of the jth voxel at the n+1

iteration. The iterations are stopped when the following convergence criteria is satisfied:

$\left|V^{n+1} - V^n\right| \le \dfrac{V^n}{100}$, where V^n is the object variance at the nth iteration. At each iteration, all

estimated concentrations are updated simultaneously. We initialize the concentration values by

assuming that they are the same at each voxel. We have also tried using different initial guesses

with similar convergence results. The algorithm typically converges in ten to twenty iterations.

In order to better understand the capabilities of the tomography algorithm in

reconstructing chemical cloud concentration distributions utilizing a limited number of views, we

considered sample objects of increasing spatial complexity as viewed by an increasing number of

sensors, and compared the reconstructed functions with the original analytical objects. We define

the metric for the goodness of reconstruction as the nearness [16] (the lower the nearness values,

the better the reconstruction):

$$0 < Nearness = \sqrt{\frac{\sum\limits_{j}^{xy}(O_j^* - O_j)^2}{\sum\limits_{j}^{xy}(O_j^* - O_{avg}^*)^2}} \leq 1 \qquad (23)$$

O_j^* = j^{th} voxel value of original function

O_j = j^{th} voxel value of reconstructed function

O_{avg}^* =   original function average value

The original analytical functions to be reconstructed are shown in Figure 8. The first function, Function A is a simple 2-D Cosine Function (Fig. 8a). Function B (Fig. 8b) and Function C (Fig. 8c) have the 2-D Cosine Function as their basis but offer increased complexity with the addition of multiple peaks. Function D (Fig. 8d) is a combination of multiple 2-D Gaussians where the symmetry axis is not normal to either of the primary axes of the grid.

We first evaluated the algorithm for two orthogonal sensor views (0 and 90 degrees) with 128 projections per view for a total of 256 projections through the object. Reconstruction of Function A yields a nearness value of 0.08. The overall shape and maximum values are well reproduced with errors less than 5%, even in the limited case of 2 sensor views. The reconstruction result is shown in Figure 9a along with the reconstruction error distribution. Function B is reconstructed with a nearness value of 0.17 and is shown in Figure 9b. The overall shape and maximum values are still well reproduced. There is however, a clear decrease in fidelity at higher spatial frequency, resulting in reconstruction errors as large as ~10%.

The reconstruction of Function C is shown in Figure 9c. As a result of the increased spatial complexity of Function C, two sensor views cannot provide sufficient projection data to enable accurate estimation of the third strongest peak of the function. It is apparent that some of the intensity is distributed along the entire estimation grid. The estimated distribution has a

nearness value of 0.38 and estimated concentrations are in error by as much as 40%. The need

for additional projection data becomes even more evident when the CT algorithm is used to

estimate Function D. In the case of only two sensors, when cloud's axis of symmetry is not

parallel to one of the viewing axes, non-zero column density measurements can only be

interpreted as increased dispersion. This effect can be observed in the reconstruction of Function

D, as shown in Figure 9d; the estimated distribution is characterized by an increased width along

one of the axes. The nearness value is 0.70 and is indicative of a low fidelity estimation;

estimation errors are as high as 50%. These errors point out the need for an additional instrument

to reduce the ambiguity in the two sensor data set.

For comparison with the two sensor simulation we added a third sensor whose line-of-

sight was oriented at 45 degrees with respect to the first two sensors and used the CT algorithm

to estimate Function D again. The estimated function is illustrated in Figure 10. The addition of

the third sensor decreases (improves) the nearness value from 0.70 to 0.27. The errors associated

with the reconstruction were reduced from ~50% to <20% and the directionality of Function D

with respect to the two orthogonal primary grid axes is now accurately estimated. As might be

expected, the addition of a fourth sensor (at 135 degrees) reduces estimation errors to < 10% and

improves the nearness value to 0.10. The reconstruction of Function D with 4 sensors is shown in

Figure 11.

In summary, our simulations lead us to conclude that the tomography algorithm cannot

accurately reproduce spatially complex clouds when only two orthogonal views are used for the

cloud reconstruction. However, for clouds approximately described by smooth varying functions

with propagation along one of the viewing centerlines, estimated synthetic cloud concentrations

were accurate to within 10% or less, even when only 2 projections views are used. The addition

of a third view significantly increases the fidelity of the reconstruction for spatially complex clouds with changing direction of propagation, resulting in errors of less 20%. From the perspective of a perfect synthetic projection data field, simulations indicate that 4 sensors may be sufficient to provide full 3-D reconstructions of chemical cloud concentrations that are accurate to within 10%, even for very complex distributions. It is important to note however, that in real field deployment scenarios, the ability of the sensors to achieve a highly accurate determination of the cloud column density is dependent on the level of air temperature to background thermal contrast encountered by the sensors from each viewing location. As a result, it is very likely that some sensors may not provide enough column density (projection) data needed to generate accurate 3-D concentration distributions.

A 4-sensor constellation may be degraded to a 3- or even a 2- sensor constellation depending on the quality of the column density measurement associated with each sensor. As a consequence, from a real world application perspective, it is important to provide a sufficient number of sensors in order to obtain quality column density data from at least 3 – 4 viewing projection angles that are needed for accurate reconstructions.

4.   Dugway Proving Ground (DPG) Field Data and Tomographic Results

The data acquired by the sensor constellation during the field trials at DPG in 2006 was based on observing explosive disseminations of glacial acetic acid (AA), tri-ethyl phosphate (TEP) and R134a. All three chemicals display unique spectral signatures in the 8 -11 µm spectral region and are amenable to standoff detection by passive infrared sensors such as AIRIS. The majority of the releases involved dissemination of between 15 kg and 120 kg of material

however three disseminations exceeded 220 kg. We present analysis of seven dissemination experiments here.

Three sensors were available for field measurements and they were deployed in the 0, 45, 90 degree configuration described in the previous section. While in principle deployment at 0, 60, and 120 degrees could enable more accurate estimation of the chemical concentration distribution, the 0, 45, 90 degree configuration had the logistical advantage that if one of the sensors failed then two sensors could be immediately deployed at the 0 and 90 degree locations without having to resurvey the deployment area, as would be necessary if moving a sensor from the 60 deg or 120 deg to 90 deg deployment position. The sensor constellation was arranged such that the field of view of each sensor was centered in azimuth on the location of the explosive releases. Each AIRIS-WAD sensor unit was located 2.8 km from grid center and the geometry defined a 0, 45, 90 degrees configuration as developed and validated using the simulation study described in the previous section. Each pixel in the image mapped to a plane ~6.0 m x 6.0 m at grid center. The absolute position of each sensor was established to centimeter-level accuracy using differential GPS measurements. Extreme care was also taken to align each sensor's field of view with fiduciary markers on the test range to ensure that the sensor views were co-planar and that the projections through the reconstruction volume were known to high accuracy. Projection angles and co-planarity are believed to be accurate to better than 1 mrad, i.e., significantly less than the single pixel IFOV, 2.2 mrad.

Figure 12 shows an example of data products generated using data acquired simultaneously by the three sensors. The cloud detected in Figure 12a (top) originated from a 120 kg burst release of acetic acid and the imagery was acquired ~ 1 minute after the burst. Acetic acid detections correspond to the white pixels near the center of each image. The

detection in Figure 12b (bottom) corresponds to a 90 kg TEP dissemination. The Adaptive Cosine Estimator (ACE), as described in Section 2, identifies and flags pixels which meet a given correlation criteria between the differential radiance spectrum and the reference spectrum of the species in the cloud. The horizontal lines in Figure 12 determine the vertical overlap boundaries within which the tomography algorithm can be applied in order to generate concentration distribution for each altitude bin (row of pixels) within the detection grid. The detection grid is defined as ~ 1.2 km x 1.2 km truth box in which all three sensors have overlapping fields-of-view. The full 3-D cloud reconstructions are obtained by stacking the concentration distributions from each altitude bin. Figure 13 illustrates the number of detected pixels from each sensor as a function of time after the initial release for both the AA and TEP disseminations shown in Figure 12. The data shows that the sensor constellation detected the chemical simulants within ~30 seconds of the release. In the case of the AA release, the cloud moved out of the sensors' fields-of-view ~2.5 minutes after the dissemination and re-entered the field-of-view of the sensor at the NE position ~80 seconds later. Typical sensor constellation detection times were approximately 5-6 minutes before the clouds cleared the detection grid. However, low wind conditions allowed some chemical releases, such as the TEP case in Figure 12b, to be detected for as long as 14 minutes. In Figure 12, the AA cloud was observed as high as 100 meters above the ground, but the TEP cloud climbed as high as ~300 meters. (As noted in Section 2, concentration values estimated at elevations hundreds of meters above ground level are likely underestimated. Calculations suggest that ΔT_{eff} (effective thermal contrast) may be overestimated by as much as 10-20% at the highest cloud elevations in Figure 12b if one assumes that the cloud temperature is equal to the air temperature at ground level; estimated concentrations would be underestimated by a corresponding amount.) Most of the detected

releases stayed relatively low to the ground due to the formation of low atmospheric inversion layers that are prevalent at DPG during the night. The background scenes observed by the sensors during the DPG releases typically provided air temperature to background radiance thermal contrast that was > 2 K. Even in cases when $1 \text{ K} < \Delta T < 2 \text{ K}$, the sensors demonstrated the capability to detect the chemical simulant clouds.

Based on detection maps obtained from each of the sensors, the chemical cloud column densities were calculated for each pixel detected using the methodology previously described. The column densities were reported in units of mg/m^2. Column density data was then used as input for the tomography algorithm in order to generate concentration values in units of mg/m^3 associated with each voxel in the 3-D grid. Furthermore, the uncertainties associated with each column density measurement were also determined and propagated through the tomography algorithm in order to generate the magnitude of the concentration error. As a consequence of the fact that the tomography algorithm is iterative and computationally intensive, and since the analysis described in this paper was performed on a slow IDL platform, we binned the sensor imagery from 256 x 256 down to 128 x 128 in order to reduce the computational time. As a result, all of the chemical cloud 3-D reconstruction had a nominal voxel volume spatial resolution of 12 x 12 x 12 meters. Given the truth box resolution, and taking advantage of observed low wind speeds (< 2 m/s) and slow moving clouds, we co-averaged datacubes over a transit time of ~ 20 seconds prior to calculation of column density maps. This approach improved overall detection statistics and increased sensor tomography overlap. We have recently implemented the tomography algorithm on an MKL C based platform utilizing a sparse matrix format, which is currently capable of processing a single 256 x 256 slice in ~ 0.3 seconds, which represents ~ 10^3 times improvement in computational speed. This recent accomplishment allows

the generation of tomographic results in near-real time. More recent deployment of the real-time system has demonstrated the ability to temporally match datacubes within a 5 second window and generate 3-D concentration distributions at a rate of 0.1 Hz. The processing period includes time for all three sensors to acquire datacubes, reduction of datacubes to $\hat{\alpha}$ values and calculation of $\hat{\rho}$ estimates at each sensor, wireless transmission of $\hat{\rho}$ values to a central processing computer, and the CT calculation at the central processing computer.

For demonstration purposes, we focus only on the acetic acid release shown in Figure 12a, and then provide a summary of the complete analysis. An example of the AA concentration distribution within the first 12 meters above the ground level is shown in Figure 14. Figure 14 is a 5 x 4 km representation of the area indicating the position of each of the sensors along with the 1.2 km square detection grid in which all three sensors have overlapping fields of view. The calculated acetic acid concentration distribution is overlaid on top of the grid display. The maximum concentration detected is ~ 175 mg/m^3. Figure 15 shows the concentration distribution within the next 12 m layer above the ground. The maximum concentration is ~ 90 mg/m^3, indicating that, in the case of the AA release, most of the chemical cloud stayed relatively low to the ground. Figure 16 shows a magnified view of the AA concentration distributions at the two elevation levels above the ground.

In order to validate the results associated with the chemical cloud concentration distributions, we conducted a mass conservation analysis for each individual release. The only known piece of information regarding the dissemination of the simulants is the amount of material released. Unfortunately, the amount of material present in the gas phase was not known precisely. While R134a is a gas at ambient temperature and 1 atm pressure, both acetic acid and TEP have relatively low vapor pressures at ambient temperature, ~16 Torr and ~70 mTorr,

respectively and it was not possible to measure the partitioning of material between the gas and liquid phase following dissemination. The amount of liquid used in the dissemination is an upper bound on the amount of material which could be present in the gas phase. The tomographic analysis of chemical releases produces concentration values (mg/m^3) for each voxel in the 3-D detection grid. Based on the spatial resolution of the sensor (dictated by the 32 x 32 degrees FOV and the 2.8 km standoff distance), the volume of each voxel was calculated. Information on the voxel concentration in conjunction with the associated volume provides knowledge of the mass of the simulant detected in each voxel. The total mass in the 3-D volume was then obtained by summing over all voxels detected as containing the simulant. This measurement was then compared to the known release mass. Figure 17 illustrates the total mass measured based on the tomographic analysis of the release shown in Figure 14a as a function of time after the burst. No data is shown after 18:02:30 because the cloud left the volume sampled by all three sensors. The errors associated with each mass measurement were calculated by propagating the column density errors through the tomography algorithm and are also indicated in Figure 17. The maximum amount of acetic acid detected is ~ 107 ± 30 kg. When compared to the actual amount disseminated during this release (120 kg), this value suggests that the sensor constellation in conjunction with the tomographic methodology is capable of accounting for ~ 90 ± 25 % of the total mass released on the test grid. The lower mass estimates at early times after the burst are the result of the inability to accurately measure the full column density as a result of the optical thickness of the clouds. The simulant column densities in these clouds cannot be determined using our established radiative transfer model. With time, the chemical cloud disperses and reaches the optically thin limit. Under these conditions, an accurate determination of the chemical column density is possible. Eventually, the cloud disperses to the point where column

densities drop below the detection limit corresponding to the detection approach described in Section 2.

Similar analyses were conducted for several of the other releases observed during the 2006 DPG trials. A summary of the mass estimates (as percentage of the total known mass released) based on the tomographic reconstruction of the chemical clouds for each of the runs is shown in Figure 18. It can be observed that for cases in which the amount of chemical simulant released was ≤ 120 kg, the tomographic constellation is capable, on average, of accounting for ~ 86% of the total mass disseminated. There were three runs which were characterized by releases greater than 240 kg of material, which resulted in average mass estimates only on the order of ~20%. Further examination of these releases indicate the formation of optically thick clouds for a significant fraction of the time in which the chemical clouds are within the detection truth box. Preliminary re-analysis of the data indicates that correcting for optical thickness effects increases the estimated mass by a factor of 2 – 3. Analysis conducted so far suggests that the average measurement error corresponding to the mass estimate calculations are on the order of 30% or less.

The 2006 DPG results demonstrate the ability of the system to account for large fraction of the chemical simulant mass released on test ranges through CT reconstruction of cloud concentration distributions. More recently however (Summer 2008), the real-time tomographic sensor constellation has been deployed in conjunction with 25 ion mobility based point sensors. We are in the process of validating the concentration results obtained from the tomographic reconstruction of standoff passive AIRIS data against the raw concentration measurements collected with the point sensors. This approach will provide a better understanding for the ability

of the proposed CT method to accurately retrieve cloud concentrations observed from true standoff ranges.

5. Conclusions

We have defined the methodology and demonstrated the ability to use passive infrared multispectral imaging to track and quantify chemical clouds via computed tomography (CT). The CT algorithm has been demonstrated to be capable of 3-D reconstruction of chemical clouds using 2-D column density data with as few as 3 sensors. Errors associated with the reconstruction methods are less than 20% even for complex chemical cloud concentration distributions. The statistical method for the calculation of chemical cloud column densities from sensor radiometric data has been experimentally demonstrated to produce chemical cloud column density values that are accurate to within ~ 10% or less. The primary source of error in the field measurements was in the determination of the local air temperature. The total measurement error for field data is estimated to be ~ 30%. Unfortunately, lack of ground truth data precludes assessment of the absolute accuracy of concentration distributions estimated from field test measurements; however, the mass closure calculations indicate that the amount of material estimated using the CT algorithm is in good agreement with the known amount of material released. The release of large amounts of simulant into small volumes during low inversion layers produced optically thick clouds. The simulant column densities in these clouds could not be determined using our established radiative transfer model. This effect led to an under-estimation of the mass detected by the system.

6. Acknowledgments

7. References

1. Col. D. Burnett, "Joint Program Manager NBC Contamination Avoidance," presentation at the JPEO-CBD Advanced Planning Briefing for Industry, 26 April 2005.

2. L. B. Grim, T. C. Gruber Jr., M. Marshall, and B. Rowland, "Chemical Cloud Tracking Systems," in *Instrumentation for Air Pollution and Global Atmospheric Monitoring*, J. O. Jensen, and R. L. Spellicy, eds., Proc. SPIE **4574**, pp. 1-6 (2002).

3. W. J. Marinelli, C. M. Gittins, and J. O. Jensen, "Sensor Performance Needs for Wide Area Hyperspectral Chemical Agent Detection," presentation at the Fifth Joint Conference on Standoff Detection for Chemical and Biological Defense, Williamsburg, VA, 24-28 September 2001.

4. W. J. Marinelli, C. M. Gittins, and J. O. Jensen, "Passive Multispectral Imaging for Standoff Chemical Detection," presentation at the MASINT Chemical Warfare Science and Technology Symposium, San Diego, CA, August 2000.

5. C. M. Gittins and W. J. Marinelli, "Remote Characterization of Chemical Vapor Plumes by LWIR Imaging Fabry-Perot Spectrometry," presentation at the Fifth Joint Conference on

Standoff Detection for Chemical and Biological Defense, Williamsburg, VA, 24-28 September 2001.

6. W. J. Marinelli, C. M. Gittins, A. H. Gelb, and B. D. Green, "Tunable Fabry-Pérot Etalon-Based Long-Wavelength Infrared Imaging Spectroradiometer," Appl. Opt. **38**, 2594-2604 (1999).

7. D. F. Flanigan, "Prediction of the limits of detection of hazardous vapors by passive infrared with the use of MODTRAN," Applied Optics **35**, 6090-6098 (1996)

8. B. R. Cosofret, C. M. Gittins, and W. J. Marinelli, "Visualization and tomographic analysis of chemical vapor plumes via LWIR imaging Fabry-Perot spectrometry," Proc. SPIE, **5584**, 112-121, October 2004.

9. D. Manolakis, D. Marden, and G.A. Shaw, "Hyperspectral Image Processing for Automated Target Recognition," Lincoln Laboratory Journal, **14**, 1, 79-115 (2003).

10. D. Verhoeven, "Limited-data computed tomography algorithms for the physical sciences," Appl. Opt. **32**, 3736 (1993).

11. R. E. Snyder, R. G. Joklik, and H. G. Smerjian, "Laser tomographic measurement in an unsteady jet diffusion flame," Annual Meeting of American Society of Mechanical Engineers, San Francisco, 10-15 December 1989.

12. M. Hino, T. Aono, M. Nakajima, and S. Yuta, "Light emission computed tomography system for plasma diagnostics," Appl. Opt. **26**, 4742-4746 (1987).

13. D. D. Verhoven, "An experimental study of the performance of an optical tomography system," in Laser Interferometry, Proc. Soc. Photo-Opt. Instrum. Eng. **1162**, 369-377 (1990).

14. R. N. Bracewell. "Strip integration in radio astronomy," Aust. J. Phys. **9**, 198-217 (1956).

15. J. Feng, "Reconstruction in Tomography from Severe Incomplete Projection Data Using Multiresolution Analysis and Optimization," in *IEEE Digital Signal Processing Workshop Proceedings[C]* (IEEE, 1996), pp. 133-136.

16. L. A. Todd and R. Bhattacharyya, "Tomographic reconstruction of air pollutants: evaluation of measurement geometries," J. Appl. Opt. **36**, 7678 (1997).

Figure Captions

1. Imaging sensor constellation for tomographic chemical cloud mapping.

2. Technical concept for Fabry-Perot imaging spectrometer. The interferometer is located in an afocal region of the optical train.

3. Schematic diagram of three layer radiative transfer model.

4. Chemical simulant identification in laboratory absorption cell.

5. ACE estimated column density vs. mass flow derived column density.

6. Error contribution to the sensor radiometric measurement; 1 µFlux/µFlik = 1 $\mu W/(cm^2\ sr\ \mu m)$.

7. Graphical representation of the reconstruction technique.

8. Test Functions for validating the reconstruction algorithm. A: 2-D Cosine Function. B: 2-D Cosine Function as basis with one additional peak. C: 2-D Cosine Function as basis with two additional peaks. D: combination of multiple 2-D Gaussians with random spatial distribution providing a propagation axis that is not normal to either of the primary axes of the grid.

9. Reconstruction results using 2 views (0, 90 degrees) and 128 projections/view a) Function A, b) Function B, c) Function C, d) Function D

10. Reconstruction of Function D with 3 sensor views (0, 45, 90 degrees).

11. Reconstruction of Function D with 4 sensor views (0, 45, 90, 135 degrees).

12. Simultaneous detection of a) Acetic Acid and b) TEP from all three AIRIS-WAD sensors.

13. Number of detected pixels for each of the sensors as a function of time after initial burst: a) 120 kg Acetic Acid release and b) 90 kg TEP release.

14. AA concentration distribution at 0-12 m elevation above ground: Contour map (left) and surface plot (right).

15. AA concentration distribution at 12-24 m elevation above ground: Contour map (left) and surface plot (right).

16. AA concentration distributions at 0 – 12 m (left) and 12 – 24 m (right) meters above ground.

17. Calculated total mass in the 3-D volume as a function of time after the initial release of 120 kg of acetic acid.

18. Mass estimation based on the 3-D tomographic reconstruction of chemical clouds for several runs (mass estimation expressed as percent of the total known mass released on the test grid).

Figures
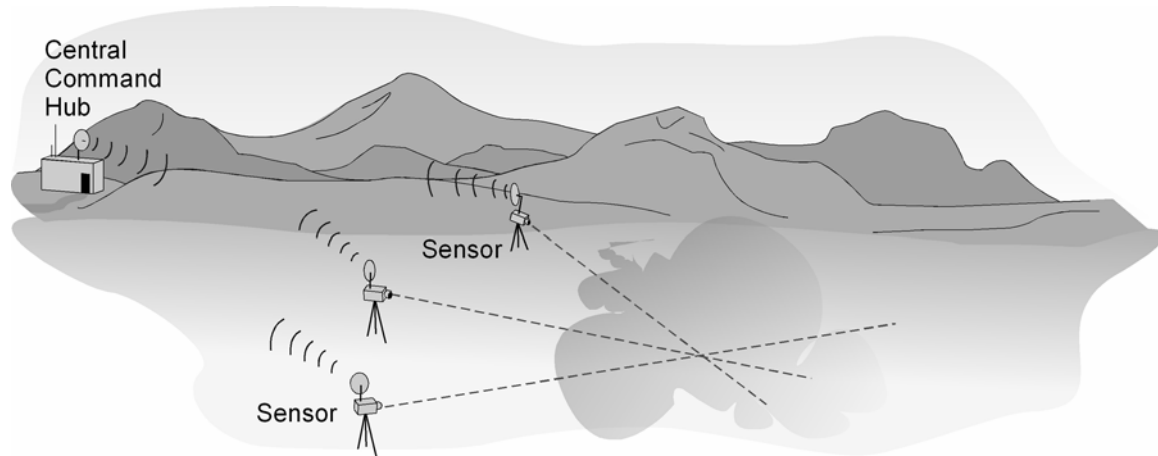
Figure 1
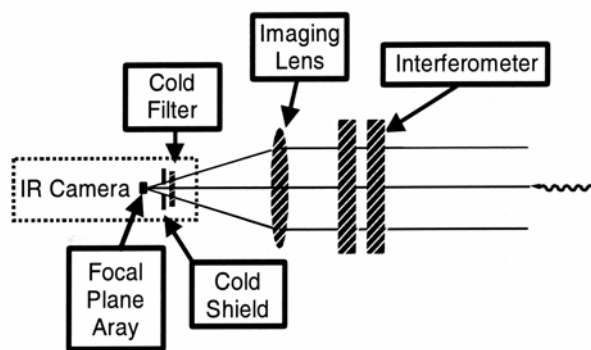
Figure 2
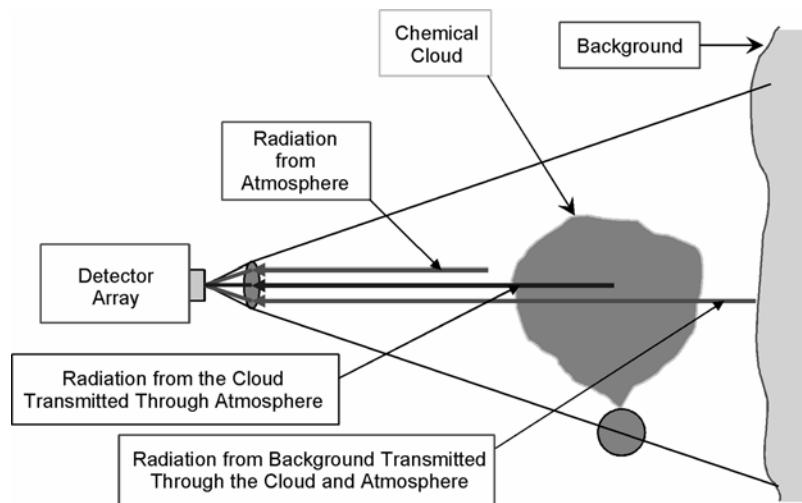
Figure 3
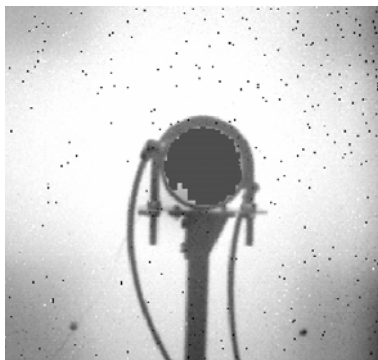
Figure 4
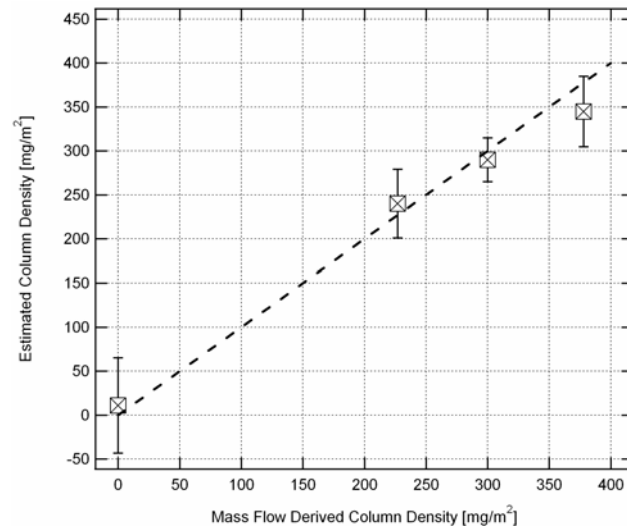
Figure 5
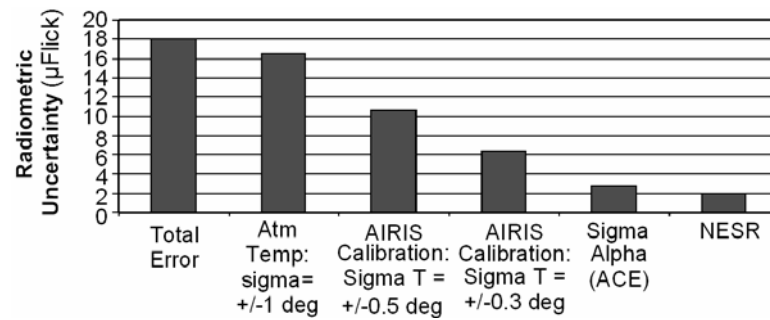
Figure 6
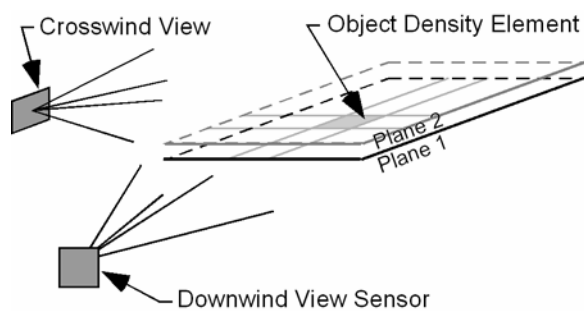
Figure 7
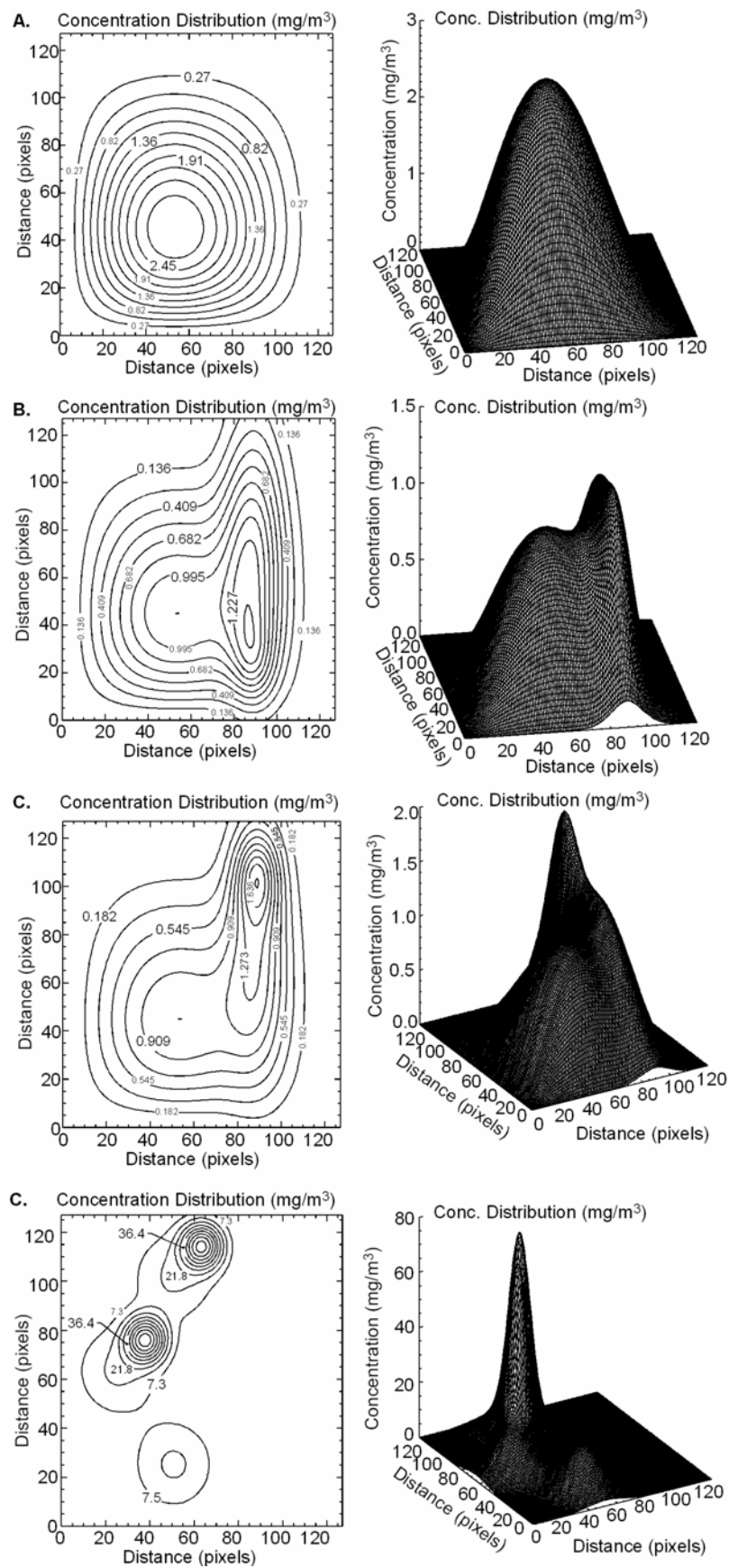
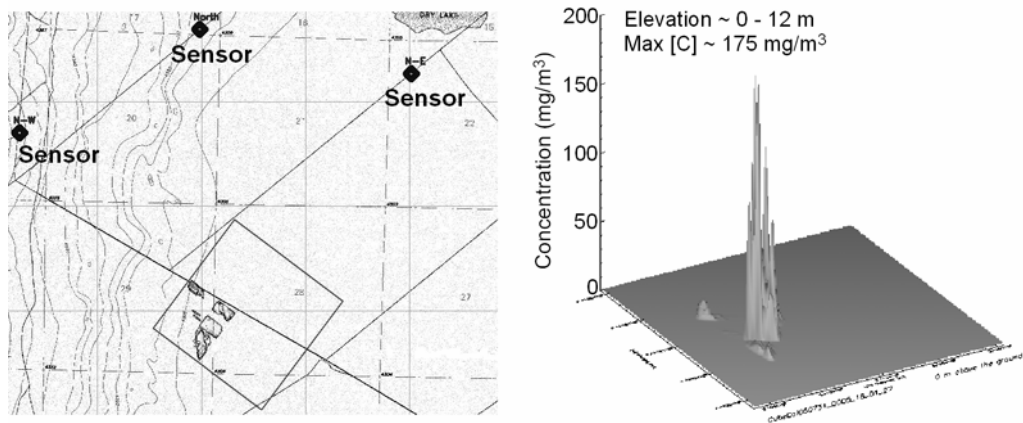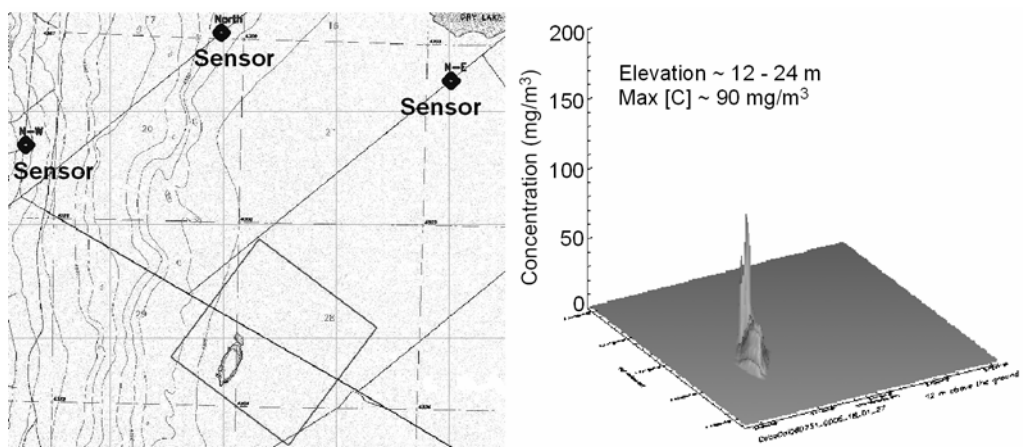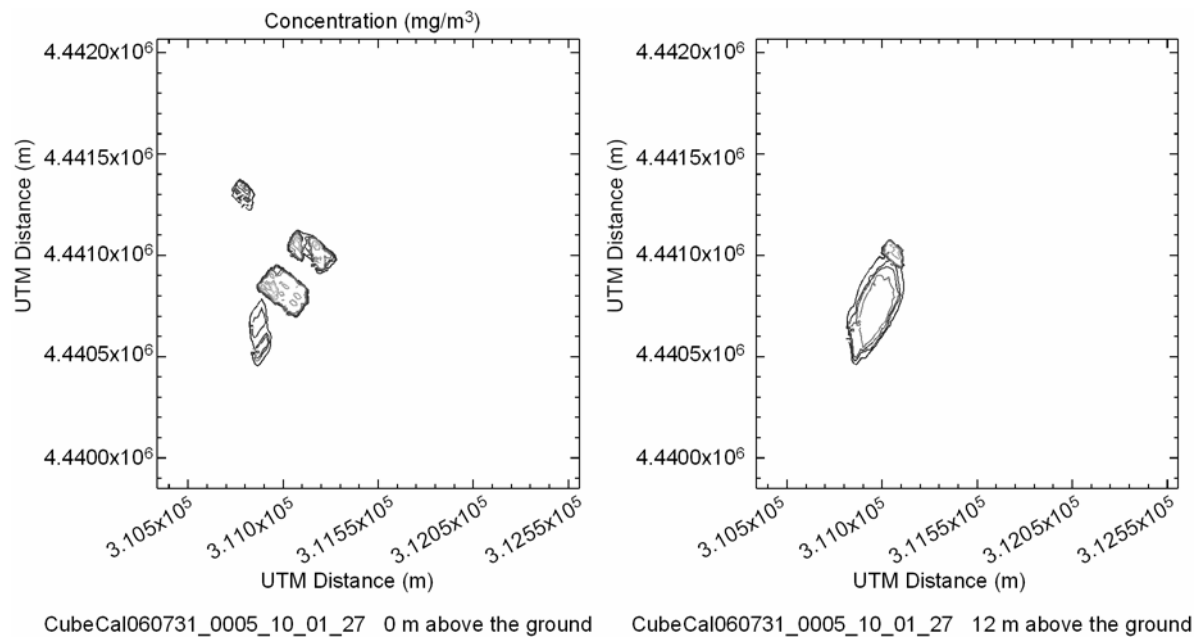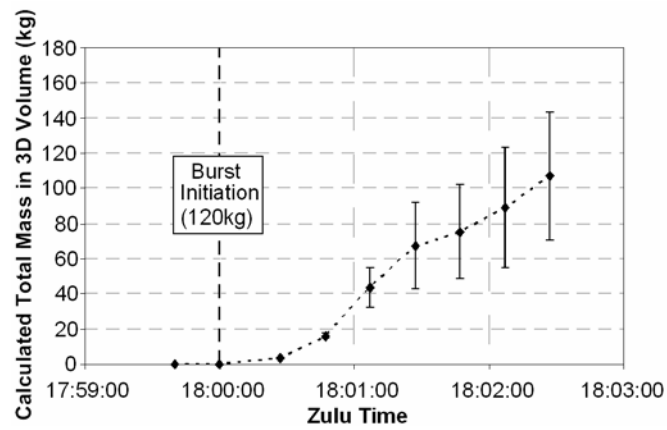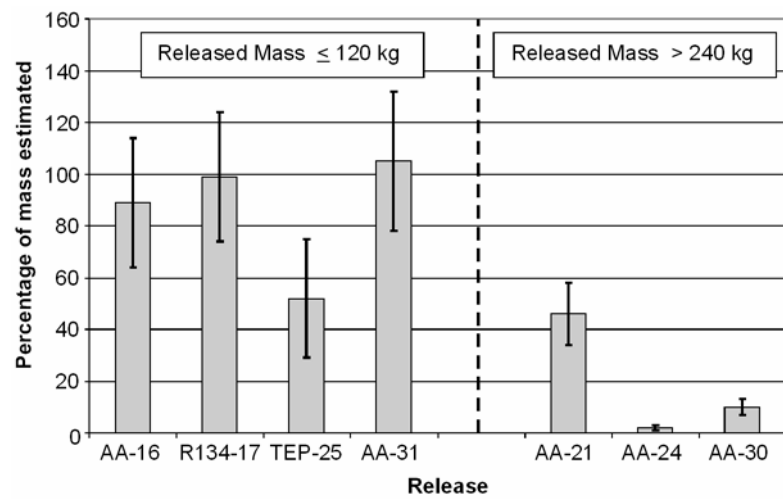**Figure 8**
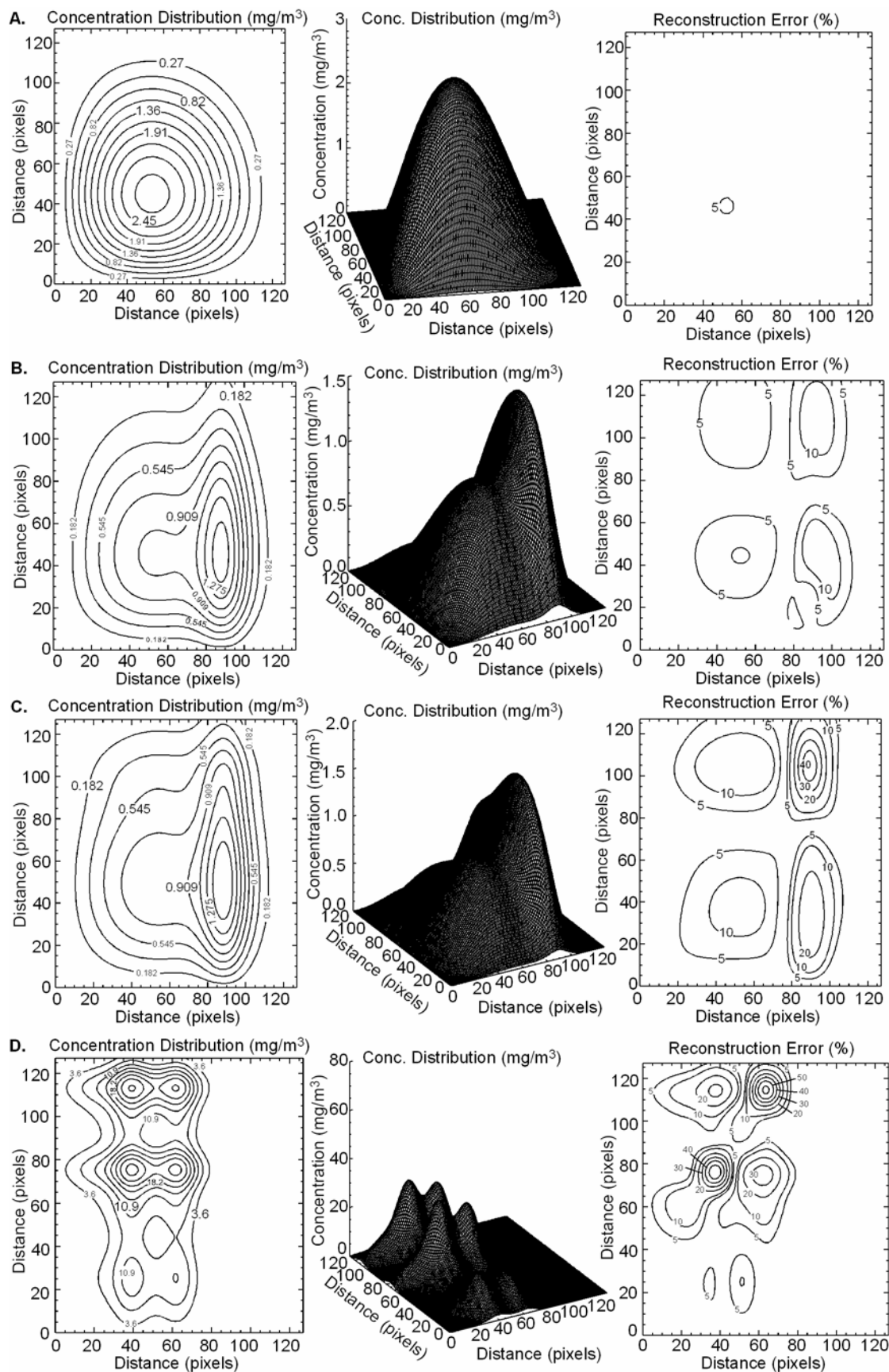
Figure 9
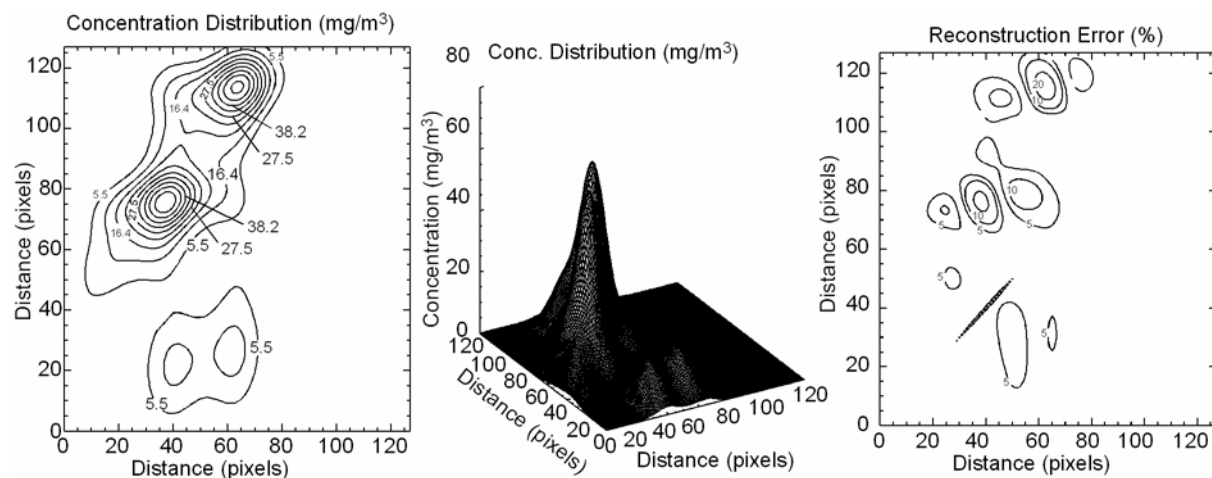
Figure 10
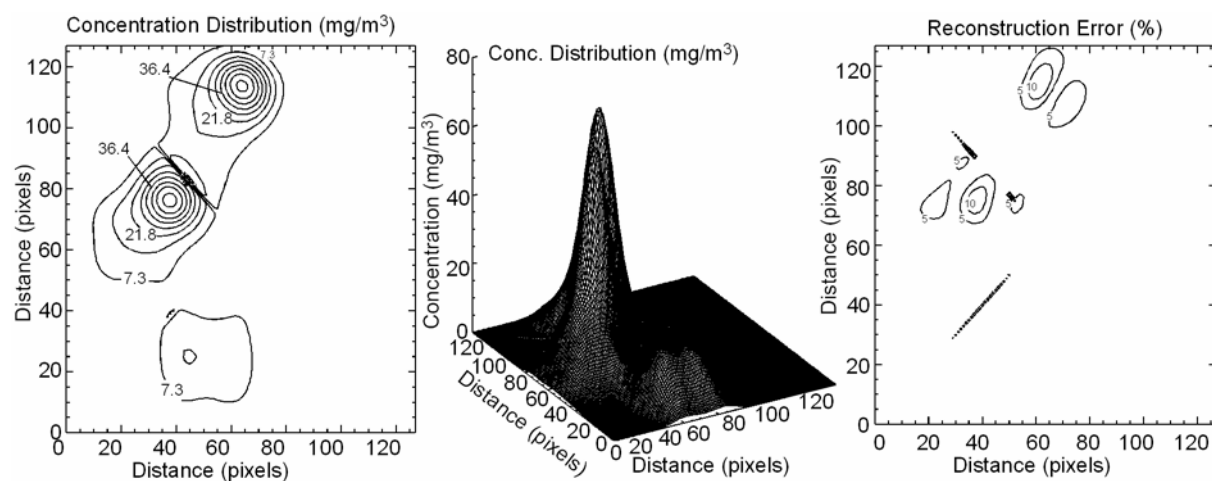
Figure 11
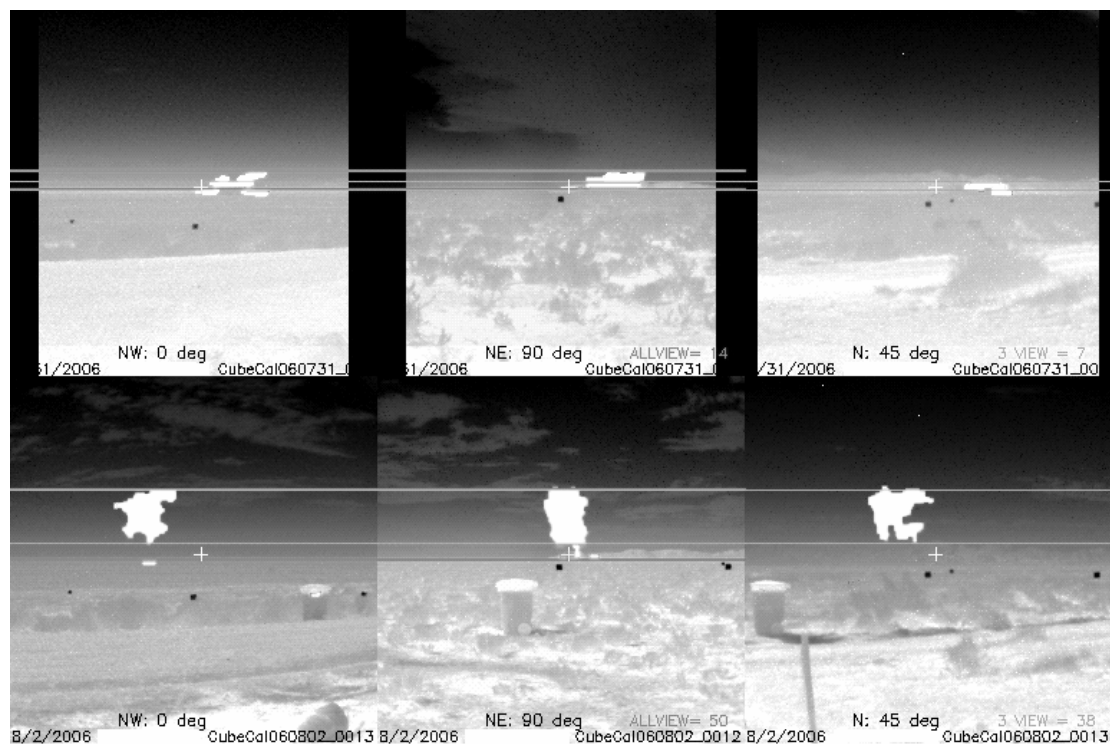
Figure 12
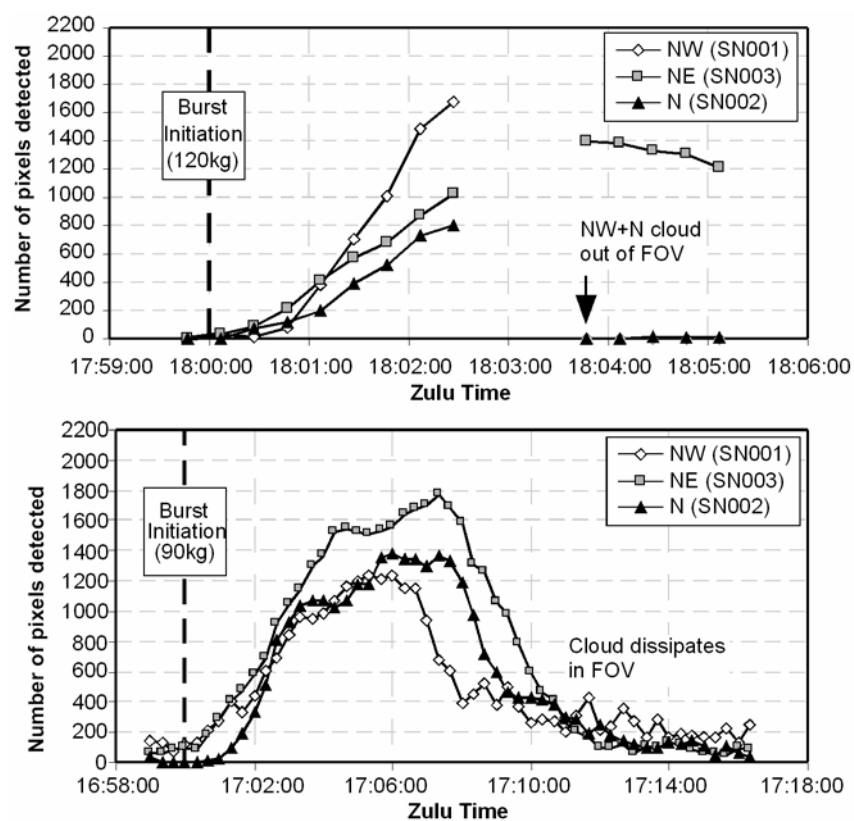
Figure 13

Figure 14

Figure 15

Concentration (mg/m³)

CubeCal060731_0005_10_01_27   0 m above the ground

CubeCal060731_0005_10_01_27   12 m above the ground

Figure 16

Figure 17

Figure 18